(Received 13 May 2024, Accepted 18 July 2024, Scheduled 31 July 2024)

Wearable Antenna System for Osteoporosis Detection and Monitoring Using Machine Learning

Eman G. Ouf[1], Anwer S. Abd El-Hameed[1, *], Asmaa G. Seliem[2], and Shaza M. Elnady[1]

[1] *Electronics Research Institute, Cairo, Egypt*
[2] *Modern University for Technology and Informaion, Cairo, Egypt*

ABSTRACT: This article presents a groundbreaking approach to osteoporosis detection and monitoring by integrating a new wearable monopole antenna design with advanced machine learning algorithm (neural network). Inspired by the intricate pattern of a Christmas snowflake, the system utilizes UWB electromagnetic waves and bone attenuation analysis for compact, noninvasive, and highly accurate bone health assessment. Fabricated entirely from textile materials, the antenna features remarkable performance metrics, including an impedance bandwidth of 4.9 to 12.6 GHz and a reflection coefficient consistently below -10 dB, within a compact form factor of 41.9 mm $\times$ 29.2 mm. Experimental validation and comparative studies demonstrate the effectiveness of this approach in precisely classifying osteoporosis levels, achieving an outstanding accuracy rate of 87%. This study signifies a significant advancement in osteoporosis detection and diagnosis, combining state-of-the-art antenna technology with advanced machine learning techniques. The developed system holds promise for early detection and personalized monitoring of osteoporosis, contributing to improved healthcare outcomes and enhanced quality of life for individuals at risk of bone-related diseases.

1. INTRODUCTION

Osteoporosis is a chronic skeletal condition characterized by low bone mineral density (BMD) and deterioration of bone tissue, leading to increased bone fragility and a higher risk of fractures [1]. It is frequently called the "silent disease" because it advances gradually over time without exhibiting any signs until a fracture occurs. The World Health Organization (WHO) states that osteoporosis is considered to have begun if a person's bone mineral density (BMD) is less than 2.5 standard deviations below that of a healthy person [2]. Osteopenia is the term for the decrease in bone mass brought on by the gradual calcium depletion in the bones. One's susceptibility to osteoporotic fracture rates rises with the severity of osteopenia. BMD is calculated by dividing the bone mineral content (BMC) by the estimated area of the bone being examined, resulting in a mass/area measurement, which is an "areal" density estimate. Therefore, bone size, BMD, and BMC are the primary indicators of osteoporotic fractures. The trabecular bone's typical structure demonstrates wideband connection, In contrast, the disorganized band in osteoporotic bone no longer adds to the bone's strength [1, 2]. The identification of osteoporosis was not attributed to one person. As a result of the efforts of numerous scientists and researchers, osteoporosis has come to be recognized as a medical problem. The first documented evidence of osteoporosis can be found in antiquated civilizations like Egypt and Greece, where the ancient Greek physician Hippocrates described symptoms resembling osteoporosis. In the early 1900s, researchers began to recognize osteoporosis as a disorder characterized by decreased bone density and a higher risk of fractures. By the mid-1900s, scientists started to differentiate between the concept of osteoporosis due to age-related bone loss and bone loss due to other underlying conditions. Diagnostic imaging techniques, like dual-energy X-ray absorptiometry (DXA), were used in the late 20th century to quantify bone density and diagnose osteoporosis. In the 21st Century, osteoporosis became a major public health concern. Today, osteoporosis research continues to advance, with a focus on prevention, early diagnosis, and improved treatment methods. Osteoporosis is expected to cause fractures in 56 million people worldwide; early identification is therefore essential to preventing fractures and successfully managing the condition. As a result, osteoporosis becomes a worldwide health concern [3, 4].

There are several imaging techniques and tests commonly used to evaluate bone density and detect osteoporosis, such as quantitative computed tomography (QCT), Quantitative ultrasonography (QUS), and dual-energy X-ray absorptiometry (DEXA). The most popular technique for identifying osteoporosis, forecasting future fracture risk, and routinely evaluating patients is DEXA scan [5, 6]. Although the bone mass can be measured using this method, it does not provide any insight into the biology, health, or composition of the bone, all of which are considered important aspects of bone quality [7, 8]. Due to variations in the soft tissue bridging the trabecular and cortical spaces, it is rarely able to distinguish between them and is prone to mistakes [9]. Another popular technique, volumetric QCT, offers densitometry analysis as well as structural components for separate cortical and trabecular bone structures. However, the assessment process is more time-consuming and exposes the patient to more radiation than DEXA, which raises cancer susceptibility. Due to uncontrollable factors in repeated assess-

* Corresponding author: Anwer S. Abd El-Hameed (anwer.sayed@eri.sci.eg).

ments, most other approaches have major drawbacks that ultimately restrict their therapeutic efficacy and render them untrustworthy.

Researchers are concentrating on a bone analyzer based on microwave technology due to the numerous shortcomings of the available technologies and their desire to minimize costs and radiation exposure [10]. It has been demonstrated that microwaves are a more cost-effective option for evaluating bone structure than DEXA and QCT. Its F is employed to demonstrate the conductive properties of human tissue and emits non-ionizing radiation, deemed safe for medical use [11]. Ultra-wideband (UWB) microwave systems are particularly ideal for bone investigation due to their extensive coverage, high resolution, and ability to penetrate human tissues, including bones [12]. Numerous noninvasive medical applications employ microwave method because of the aforementioned benefits [13, 14]. Even though a lot of effort has been put into the construction of a microwave-based bone analyzer, more thorough data processing and classification is still necessary [15, 16]. A microwave imaging system was suggested in one instance to examine the calcaneus bone; however, the research was restricted to identifying fractures [17]. It has also been suggested to use implantable microwave devices to track how quickly damaged bones recover [18].

A monopole is a common design that has always been used to achieve UWB due to its simplicity and efficiency. A monopole, a radio antenna variant, comprises a solitary conductive element that extends vertically from a ground plane or conductive surface. The monopole antenna's length usually corresponds to the frequency of the signal that it is intended to broadcast or receive, and is expressed as a quarter wavelength or a multiple thereof. Due to their omnidirectional radiation pattern and ease of installation, monopole antennas are widely utilized in many different applications, including mobile communications systems, broadcasting and wireless networks [19]. Their versatility and effectiveness made it appropriate to use them to realize the main objective of this research

A wearable antenna is an apparatus that is worn on the body, engineered for either receiving or transmitting electromagnetic waves. It can be used in various applications such as wireless communication, satellite communication, and RFID systems. Textile antennas are a popular type of wearable antenna. The antennas are woven into fabric and can be used in wearable garments such as jackets or hats. They can be seamlessly integrated into clothing, offering flexibility and convenience [20]. The combination of wearable antenna technology with machine learning algorithms holds great potential for enhancing the accuracy and accessibility of osteoporosis screening and monitoring in clinical settings. Continued research and development in this area will further refine and validate this integrated approach, ultimately leading to improved patient outcomes and advancing healthcare practices.

In this paper, a new wearable monopole antenna design inspired by the intricate pattern of a Christmas snowflake is proposed as a sensor for osteoporosis detection. The proposed sensor uses UWB electromagnetic waves to analyze bones and classify bone health. The attenuation through bones of different masses is recorded. Furthermore, this paper integrates machine learning algorithms into the classification process, enhancing the accuracy and efficiency of osteoporosis detection. By combining data from the wearable sensor with advanced machine learning techniques, we achieve robust classification of bone health status. The subsequent sections of this paper are organized as follows. Section 2 presents the proposed sensor, detailing its design geometry, fabrication process, and outcomes. In Section 3, the operational principles are discussed, along with a comprehensive overview of the microwave system and the types of bone samples utilized for classification. A comparative study of the experimental results of propagation delay through the bones that varies with permittivity is covered in Section 4. Section 5 presents osteoporosis classification and prediction based on neural network. The conclusion of the paper is provided in Section 6.

2. THE RECOMMENDED SENSOR

The primary goal of this research is to design and implement a textile UWB antenna with a simple design and novel shape for bone health examination. Accordingly, the monopole design is chosen because it is widely used in a variety of applications due to its simplicity and efficiency, provides an omnidirectional radiation pattern, and is easy to install. The textile antenna, a type of wearable antenna, is also chosen because it can be seamlessly integrated into clothing, providing flexibility and convenience. The proposed antenna resembles a Christmas snowflake and will be used as a sensor to detect osteoporosis.

2.1. Design Geometry

Figure 1 displays the design geometry of the recommended sensor. The sensor design is based on a traditional circular disc antenna [21–24]. The circular shape has been modified into a fractal shape to miniaturize the size while maintaining the same operating bandwidth by increasing the current path within a smaller area. The Christmas snowflake monopole shape is chosen for its compactness. To achieve UWB impedance matching, a coplanar waveguide feed with a taper technique is integrated. It is worth noting that the entire antenna is designed on textile materials, using conductive fabric nanoparticle with surface sheet resistance of 0.05 Ohm/square for the radiating el-

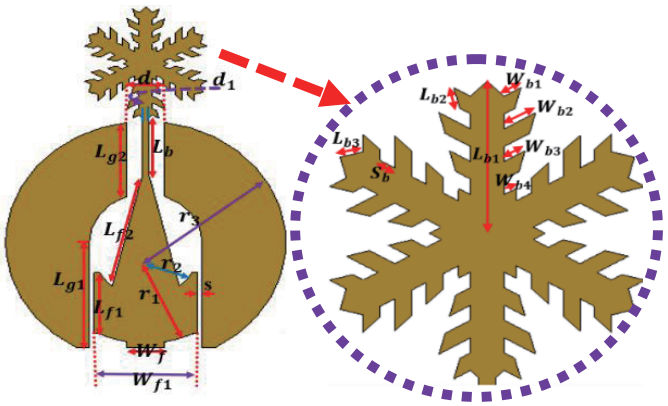

FIGURE 1. Geometry of the introduced antenna.

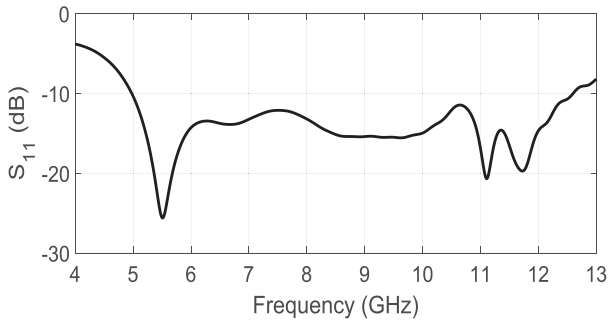

FIGURE 2. Simulated S_{11} versus frequency.

TABLE 1. Optimized dimensions for the proposed sensor (in mm).

Parameter	*Value*	*Parameter*	*Value*	*Parameter*	*Value*
W_f	4	r_1	12.4	W_{b1}	0.8
W_{f1}	11	r_2	6	W_{b2}	1.49
L_{f1}	7.5	r_3	14.9	W_{b3}	0.99
L_{f2}	14.06	S	0.5	W_{b4}	0.56
L_{g1}	12.9	L_{b1}	7	S_b	0.69
L_{g2}	9.11	L_{b2}	0.99	d	4
L_b	7.05	L_{b3}	0.98	d_1	0.7

ement and cotton material for the substrate. The material has a dielectric constant of $\varepsilon_r = 1.8$ and a $\tan\delta$ value of 0.025. The overall optimized dimensions are tabulated in Table 1. Figure 2 presents the simulated reflection coefficient versus frequency which shows a good matching below -10 dB starting from 4.9 GHz to 12.6 GHz.

Figure 3 presents the 5 GHz, 7 GHz, 8 GHz, and 9 GHz electric field distributions of the suggested sensor in order to provide a deeper knowledge about its working mechanism. It is evident that different parts of the sensor are responsible for its radiation at each frequency.

The proposed snowflake UWB antenna design evolves through three stages, as shown in Figure 4(a). It begins with a simple circular monopole (Ant.1), then adds four arms to create a cross shape (Ant.2), and finally develops into an intricate snowflake pattern (Proposed). This progression aims to enhance the antenna's performance, which is evident in the reflection coefficient (S_{11}) shown in Figure 4(b). The graph demonstrates that each iteration improves the antenna's characteristics, with the proposed snowflake design achieving significantly lower S_{11} values across a wider frequency range, especially between 4.9 and 12.6 GHz. This improvement indicates better impedance matching and radiation properties, making the snowflake structure particularly effective for UWB applications. The design's evolution showcases how geometric modifications can substantially impact an antenna's bandwidth and efficiency.

2.2. Bending Effect

As the antenna is placed around a human arm, there will be restrictions concerning its ability to bend. To evaluate the effect of these bends on the performance of the antenna, we have created a version of the antenna in a cylindrical shape. This allows us to investigate how well the antenna can maintain the desired operating bandwidth under different curvatures. Figure 5(a) shows the illustrations of various scenarios where the antenna is curved into a cylindrical shape, along with the corresponding results. This test examines different cylinder radii, namely 30 mm, 50 mm, and 70 mm. Figure 5(b) shows the relationship between curvature and simulated S-parameters. In the flat configuration, the bandwidth of the antenna is between 4.9 and 12.6 GHz. Within the frequency around 10.5 GHz, a minor mismatch is seen when a simulated cylinder is bent with a radius of 70 mm. On the other hand, the effect of bending is lower when the bending radius is reduced to 30 mm. The comparatively small changes in bandwidth before and after bending show how resilient the suggested textile antenna is to the effects of bending.

2.3. Fabrication and Results

Using the design parameters outlined in the prior section, a prototype of the proposed sensor is fabricated using textile materials, employing conductor fabric for the radiating element and cotton material for the substrate. A vector network analyzer (ROHDE & SCHWARZ ZVA 67) is utilized to measure the input impedances and reflection coefficient of the manufactured arrays. Figure 6 shows a photograph of the manufactured prototypes of the proposed sensor design. The comparison between simulated and experimental reflection coefficients for the sensor design is illustrated in Figure 7. A reasonable agreement is shown between the measured and simulated findings. The observed differences between the simulated and measured results can be attributed to a number of textile antenna-specific factors that were not taken into consideration during the simulation phase, including manufacturing tolerances, the effects of soldering on the SMA, and the potential influence of twisting connectors and cable movement. An impedance bandwidth (S_{11} less than -10 dB) is found to span from 4.9 GHz to 12.6 GHz, according to the simulation results. The measured bandwidth spans from 4.6 GHz to 12.3 GHz with satisfactory impedance matching of 7.7 GHz.

Table 2 provides a comparison between the proposed sensor and state-of-the-art designs. While the proposed antenna may not be as small or have as wide a bandwidth as some existing designs, it is important to emphasize that our design stands out for its low specific absorption rate (SAR) and high sensitivity compared to others in the literature. These advantages should not be underestimated, as they can greatly impact the overall performance and safety of the antenna system. Showcasing these key benefits can highlight the distinct value that the proposed design offers.

2.4. Specific Absorption Rate Evaluation

The SAR measurement, which quantifies the radiation absorbed by human tissue, is used to ensure the safety of the wearable antenna and protect the patient from potential health risks. The assessment uses SAM head phantoms and a flat phantom for body measurements, complying with International Elec-

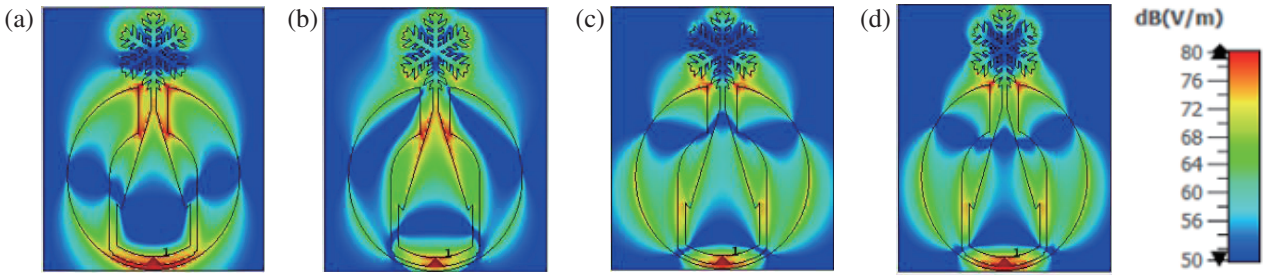

FIGURE 3. Electric field distributions of the proposed design at (a) 5 GHz, (b) 7 GHz, (c) 8 GHz, (d) 9 GHz.

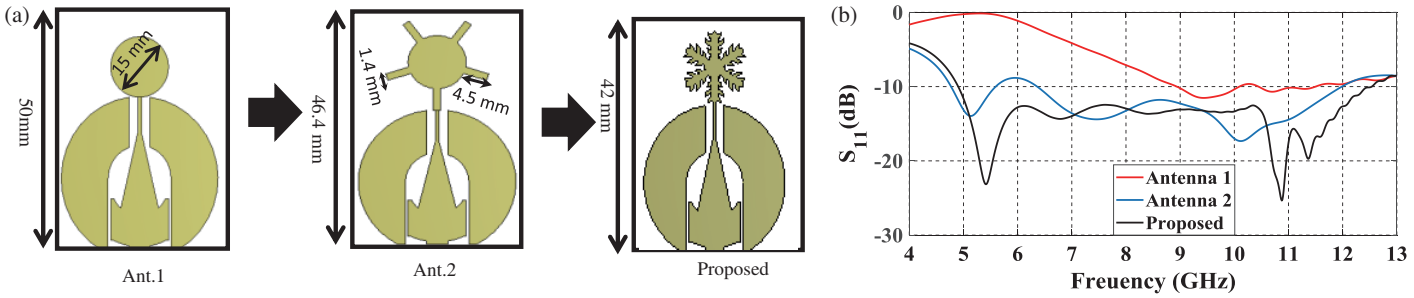

FIGURE 4. (a) Design steps. (b) Reflection coefficient versus frequency.

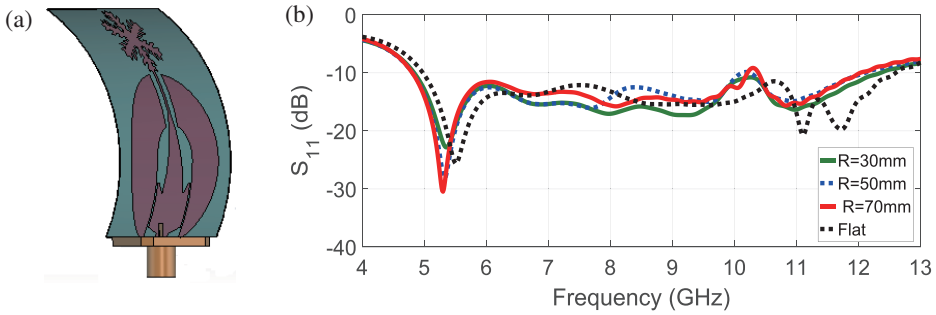

FIGURE 5. The simulated S-Parameters of various bending radii with cylinder modes in terms of. (a) Simulation Setup. (b) Simulated S_{11}.

FIGURE 6. Photograph of the fabricated sensor.

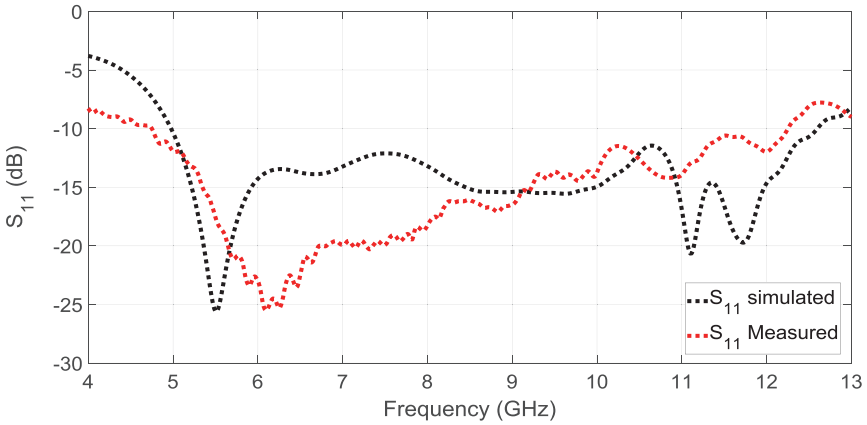

FIGURE 7. The simulated and measured reflection coefficients of the proposed sensor.

trotechnical Commission (IEC) and Federal Communications Commission (FCC) standards. Accurate SAR measurements are made using Speag Switzerland's cSAR3D, which provides quick and consistent results within 0.3 seconds and a reproducibility margin of 0.1 decibels, over a frequency range of 0.65 to 6 GHz. Figure 9 displays the SAR measurement setup for the wearable antenna. The Electronics Research Institute's central laboratories evaluate the antenna's SAR at various power

TABLE 2. Comparative analysis using previously published studies.

Ref.	[25]	[26]	[27]	[28]	proposed
Antenna type	Implantable monopole	Antipodal Vivaldi	Microwave ring resonator	Planar monopole	Snow flake fractal monopole (wearable)
Operating frequency	165 to 875 MHz	2 to 12 GHz	2.45 GHz	2.45 GHz	4.9 to 12.5 GHz
Dimensions (mm ×mm)	54.9×64.9	22×22	80×114	32×30	41.9×29.2
Sensitivity	Moderate	Moderate	High	Moderate	High
SAR (W/Kg)	N/A	N/A	< 1.6	< 0.812	< 0.1
Expremental validation done	yes	yes	yes	yes	yes
Requirement of an additional processing unit	No	yes	yes	No	yes

TABLE 3. Comparing measured SAR values for the suggested wearable monopole antenna.

Textile Monopole Antenna		*Power Level*	*Resonant Frequency*
10 g (W/kg)	*1 g (W/kg)*	*(dBm)*	*(GHz)*
0.024	0.081	0	5
0.031	0.169	5	5
0.043	0.191	10	5
0.111	0.580	15	5
0.019	0.091	0	6
0.027	0.098	5	6
0.085	0.334	10	6
0.253	0.965	15	6

levels. According to [28, 29], the antenna is considered safe if its maximum SAR emission is below 1.6 W/kg. The measured SAR values at 4 GHz and 6 GHz for the proposed textile antenna are provided in Tables 3.

3. OPERATING PRINCIPLE OF OSTEOPOROSIS DETECTION

A microwave signal passing through bone is altered (reflected, refracted, and attenuated) as a result of the electrical characteristics of the bone sample. Nonetheless, because bone tissue consists of bone minerals embedded in soft tissue, it is highly inhomogeneous and has anisotropic properties, which makes it challenging to accurately characterize bone electromagnetically. The loss of bone mineral content in osteoporosis results in a decrease in the ratio of bone volume to total volume (BV/TV). This ratio is frequently employed as a gauge for osteoporosis onset and development. As mentioned in (1), some researchers have tried to determine the conductivity and dielectric constant of bone tissue as a function of BV/TV [30, 31]. Conductivity (σ) shows a linear decrease with respect to bone density.

$$\frac{BV}{TV} = \sigma \tag{1}$$

Hence, the transmission and reflection coefficients of the microwave sensors can be affected, serving as useful indicators of the osteoporosis level.

3.1. Modeling Osteoporosis Detection

As osteoporosis is indicative of BMD, it is essential to select a body part that directly reaches the bone for accurate measurement. In this regard, we chose a body area where the bone's cross-sectional area predominates over other tissues like skin, fat, and muscles. Muscles, with a high permittivity of 47.8 and a loss tangent of 0.33267 at 6.3 GHz due to their water content, effectively attenuate electromagnetic signals and store more energy. Consequently, minimal energy is received at the receiving antenna for assessing osteoporosis levels. Therefore, the human wrist was chosen as the location to assess bone health. As shown in Table 4, Amin et al. published in vitro permittivity and conductivity data of human bone from an osteoporotic patient [32].

Based on the previously published relative permittivity and conductivity values for both healthy and osteoporotic bones, a simulation analysis of the human wrist structure was carried out using CST Microwave Studio. Figure 8(a) illustrates two identical sensors, placed on a cylindrical human wrist model, for transmitting and receiving electromagnetic signals. The cross

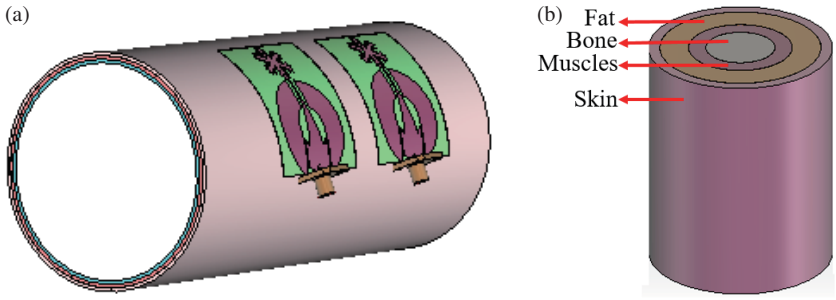

FIGURE 8. (a) Simulated model for osteoporosis detection. (b) Cross section of the human wrest.

TABLE 4. Parameters of electrical properties used to study human bone tissue at 6.3 GHz.

Tissue	*Bone*						*Muscle*	*Fat*	*Skin*
	Healthy	*Osteopenia*	*Ost. 1*	*Ost. 2*	*Ost. 3*	*Ost. 4*			
Relative Permitivity (ε_r)	9.4543	14	18	23	28	32	47.801	4.9087	34.683
Loss tangent	0.38487	0.2040	0.2374	0.2488	0.275129	0.30315	0.33267	0.18965	0.3424
Conductivity (S/m)	1.2772	1	1.5	2	2.7	3.4	5.5818	0.32677	4.1684
Radius/Thickness (mm)	15	15	15	15	15	15	4	6	2

section of the human wrist model is depicted in Figure 8(b), comprising bone tissue along with skin, muscle, and fat [33]. In the simulation software, built-in bio-tissue characteristics and dielectric properties of healthy bones, skin, fat, and muscles were considered, utilizing the biological tissues database from the Italian National Research Council [34]. Table 4 [9, 33] lists several osteopenia and osteoporotic bone characteristics that were chosen for 6.3 GHz investigation. Skin tissue, measuring 2 mm in thickness and possessing a relative permittivity of 34.683 and a loss tangent of 0.3424, makes up the outermost layer of the human wrist. There is a 6 mm thick layer of fat tissue with a loss tangent of 0.18965 and a relative permittivity of 4.9087 behind the skin layer. Following the fat layer, there is a 4 mm thick layer of muscle tissue with a relative permittivity of 47.801 and a loss tangent of 0.33267. These layers of skin, muscle, and fat surround the layer of bone tissue with 15 mm radial dimension.

To illustrate the varying degrees of osteoporosis, six distinct stages were considered [33]. Initially, there is the stage of healthy bone, characterized by a loss tangent of 0.38487 and a relative permittivity of 9.4543, indicating robust tissue connectivity. The subsequent stage is osteopenia, where the bone weakens slightly compared to wholesome bone, with a relative permittivity of 14 and a loss tangent of 0.2040. The degradation progresses with osteoporotic bone 1, marked by increased porosity, featuring a relative permittivity of 18 and a loss tangent of 0.2374. This degradation continues with osteoporotic bones 2, 3, and 4, exhibiting relative permittivity values of 23, 28, and 32, respectively, along with corresponding loss tangent values of 0.2488, 0.275129, and 0.30315, respectively. In the final stage, osteoporotic bone 4, the bone structure is severely compromised, leading to significant weakness and susceptibility to fractures. As osteoporosis progresses and bone mineral density decreases, the electrical metrics including permittivity and loss tangent demonstrate proportional rises.

3.2. Simulation Results

In the analysis of S-parameters for osteoporotic cases, significant variations are observed in both phase and magnitude across different frequency bands. Notably, as osteoporosis progresses from milder to severe stages, a notable frequency shift in S_{11} to lower frequencies is observed, decreasing from 5 GHz to 4.2 GHz as shown in Figure 9(a). This shift indicates alterations in the resonant behavior of the system, potentially attributed to changes in bone density and electromagnetic properties. Additionally, in Figure 9(b) variations in phase occur across the frequency spectrum, reflecting the complex interaction between electromagnetic waves and bone tissue. These changes in reflection coefficients provide valuable insights into the electromagnetic response of bone structures at different stages of osteoporosis, aiding in the diagnosis and characterization of the condition.

Similar to the observations in S_{11}, significant variations are noted in the transmission coefficient S_{21} across different stages of osteoporosis as illustrated in Figure 10. As osteoporosis progresses from milder to severe stages, there is a discernible shift in the frequency response of S_{21} towards lower frequencies, ranging from 4 GHz to 5 GHz as in Figure 10(a). This shift indicates alterations in the transmission characteristics of the bone tissue, potentially influenced by changes in bone density and electromagnetic properties. Moreover, variations in phase are evident across the frequency spectrum, reflecting the evolving interaction between electromagnetic waves and bone structures as shown in Figure 10(b). These changes in S_{21} provide valuable insights into the transmission properties of bone tissues at different stages of osteoporosis, contributing to the understanding and diagnosis of the condition.

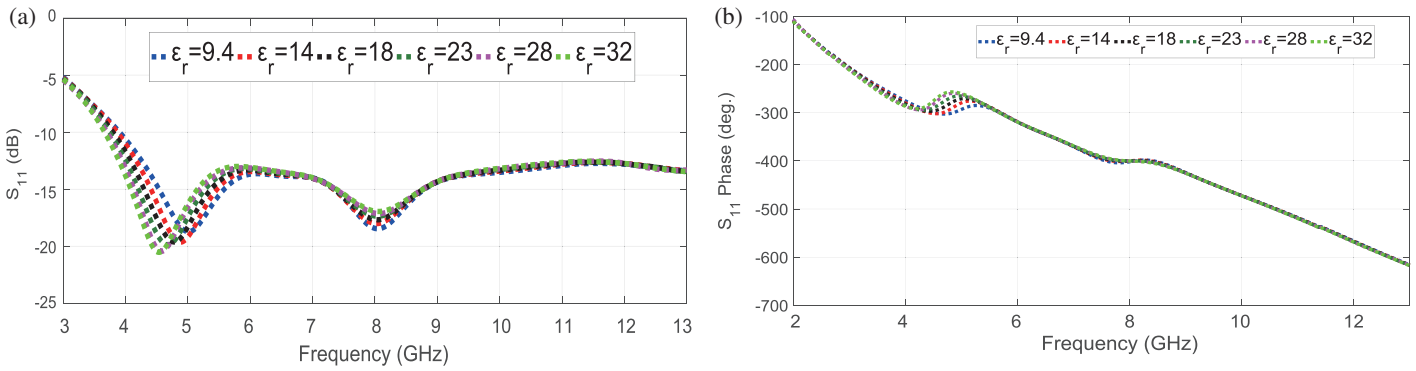

FIGURE 9. Reflection coefficients versus frequency for different levels of osteoporosis. (a) Magnitude. (b) Phase.

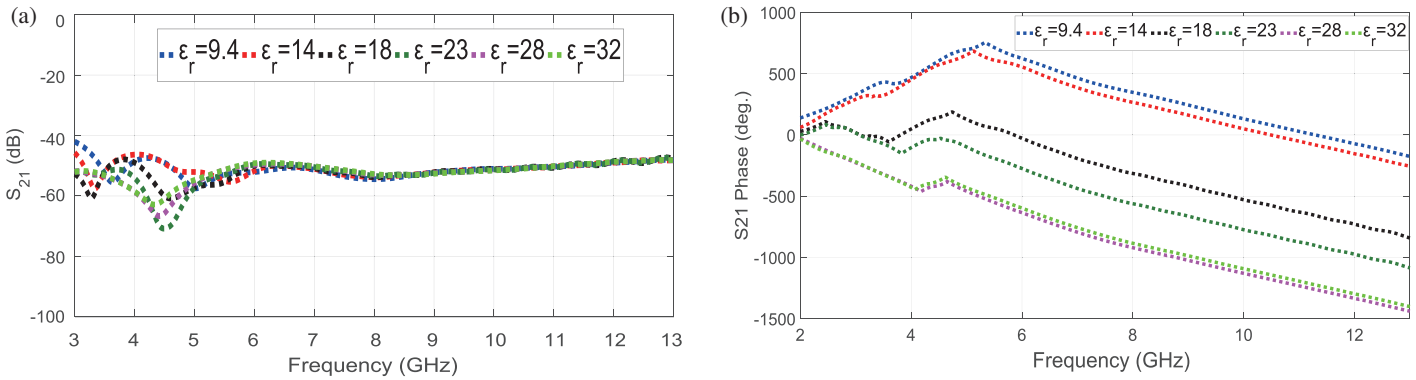

FIGURE 10. Transmission coefficients versus frequency for different levels of osteoporosis. (a) Magnitude. (b) Phase.

4. SYSTEM VALIDATION

4.1. System Description

Figure 11 shows a block diagram illustrating a microwave system proposed for generating electromagnetic waves to traverse through the test object, namely the human wrist, and analyzing the resulting attenuated transmission characteristics to evaluate bone health. The microwave signal originates from a source, undergoes amplification via a power amplifier, and is subsequently transmitted through the proposed textile monopole antenna, designed to operate within the frequency range of 4.9 to 12.6 GHz. The test object is illuminated by the textile monopole antenna's electromagnetic field. A similar monopole antenna processes the microwave signal that is received, and a low noise amplifier reduces noise before sending it to the processor for final evaluation. For simplicity, Vector Network Analyzer (VNA) is employed as the primary testing tool instead of the previously mentioned system.

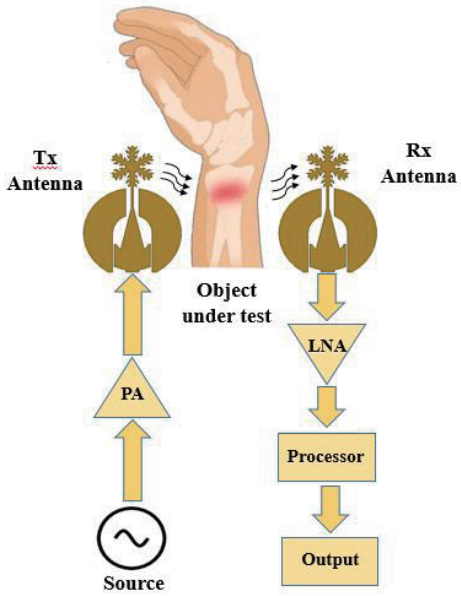

FIGURE 11. Bone health analysis microwave system architecture and operating principle.

4.2. Measurement Results

We employed the identical system setup described in the previous subsection to conduct experimental trials involving several volunteers exhibiting varying degrees of osteoporosis from healthy to Ost. 3. In this section, we will show only the results of four volunteers for verification. During these experiments, we captured the phase and magnitude of the S-parameters to assess the electromagnetic response of the bone tissue across different osteoporotic conditions. The volunteers were organized in ascending order from the healthiest individual to the severest case (Ost. 3). Figure 12 shows the measurement setup. As presented in Figure 13, the analysis of S_{11} parameters revealed a distinct frequency shift towards lower frequencies,

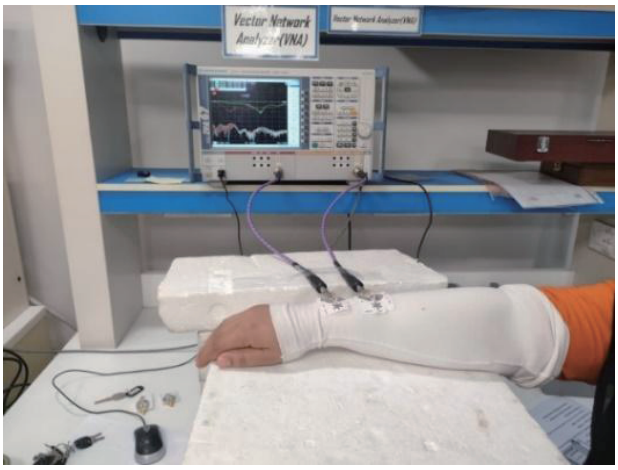

FIGURE 12. Measurement setup.

ranging from 5 GHz to 3.5 GHz, alongside noticeable alterations in phase. Additionally, in the S_{21} parameters, indicative changes were observed as in Figure 14, further highlighting the impact of osteoporosis on the electromagnetic response of the bone tissue.

5. OSTEOPOROSIS CLASSIFICATION AND PREDICTION

A novel approach to osteoporosis classification and prediction using machine learning algorithms, specifically neural networks, has been presented in this section.

5.1. Utilizing Machine Learning Techniques for Enhanced Data Analysis and Diagnostic Accuracy

In order to optimize the data collection process and enhance the accuracy of the diagnostic results, machine learning techniques were incorporated into the analysis of the dataset. By leveraging machine learning algorithms, the model can efficiently process the entirety of the dataset at once, utilizing all 801 samples per parameter to obtain a more comprehensive understanding of the electromagnetic interactions. This approach not only streamlines the detection process but also ensures that the model benefits from the full spectrum of frequency domain information, leading to more precise and reliable diagnostic outcomes.

Additionally, the dataset is further refined through the division into patches, allowing for the examination of localized variations within the frequency spectrum. Each patch captures a specific subset of the frequency range and is characterized by averaging the relevant data points within the subset. This segmentation strategy enhances the dataset's granularity, enabling a more detailed analysis of the electromagnetic properties and localized phenomena. With a total of 6408 data samples categorized into negative (healthy) and three positive levels (Ost. 1, Ost. 2, and Ost. 3), the model is equipped with a diverse and robust dataset to effectively distinguish between different health conditions of the wearer's wrist based on the electromagnetic interactions collected by the wearable antenna system.

The dataset used in this study consists of complex scattering parameters (S-parameters) obtained from a wearable system comprising two textile antennas: a transmitter (Tx) and a receiver (Rx) as described in the previous section. These antennas are strategically positioned on the human wrist, allowing for the measurement of reflections and transmission coefficients. The dataset encompasses S_{11} (reflection coefficient at Tx), S_{21} (transmission coefficient from Tx to Rx), S_{12} (transmission coefficient from Rx to Tx), and S_{22} (reflection coefficient at Rx) parameters. Each parameter is depicted by both real and imaginary components, yielding a total of eight features per data point. Moreover, to capture the intricate electromagnetic interactions comprehensively, the dataset is sampled across a frequency range extending from 2 GHz to 12 GHz, resulting in 801 samples per parameter. It should be notice that the model does not need to input data 801 times individually during the detection process. Instead, all 801 samples per parameter are simultaneously used as part of a single, comprehensive input vector for each diagnostic instance. This means that for each diagnostic evaluation, the model processes the entire dataset at once, leveraging the full spectrum of frequency domain information to produce a more accurate and reliable diagnostic result. This frequency range provides valuable insights into the electromagnetic behavior of the system and its interaction with the human wrist. Furthermore, to enhance the dataset's granularity and capture localized variations, the data are divided into patches. Each patch represents a contiguous subset of the frequency spectrum, allowing for the examination of localized phenomena within the broader frequency range. The value of each patch is established by averaging the relevant data points within the subset, facilitating a more detailed analysis of the electromagnetic properties. For simplicity, the proposed model depends on 6408 data samples divided into four categories, ensuring diversity and robustness in the dataset. The first category is negative which is healthy, while the other three categories are positive and have the levels of Ost. 1, Ost. 2, and Ost. 3.

5.2. Neural Network Model Architecture

For the prediction of osteoporosis levels using the complex S-parameter dataset, we employ a Complex Neural Network architecture. As seen in Figure 15, this neural network has numerous levels, including input, hidden, and output layers, in order to handle the complex nature of the dataset. The input layer of the neural network consists of 8 nodes, corresponding to the eight features extracted from the complex S-parameter data. The hidden layers are constructed with a hierarchical distribution of neurons, with a configuration of [512, 256, 128]. This indicates that the first hidden layer contains 512 neurons; the second hidden layer contains 256 neurons; and the third hidden layer contains 128 neurons. Rectified Linear Unit (ReLU) activation functions are applied to each hidden layer, allowing for the incorporation of non-linearity and empowering the network to discern intricate patterns present in the data. Dropout layers are integrated to address overfitting concerns by randomly deactivating a portion of neurons during training, enhancing the model's ability to generalize. Finally, the output layer comprises four nodes equal to the number of osteoporosis levels,

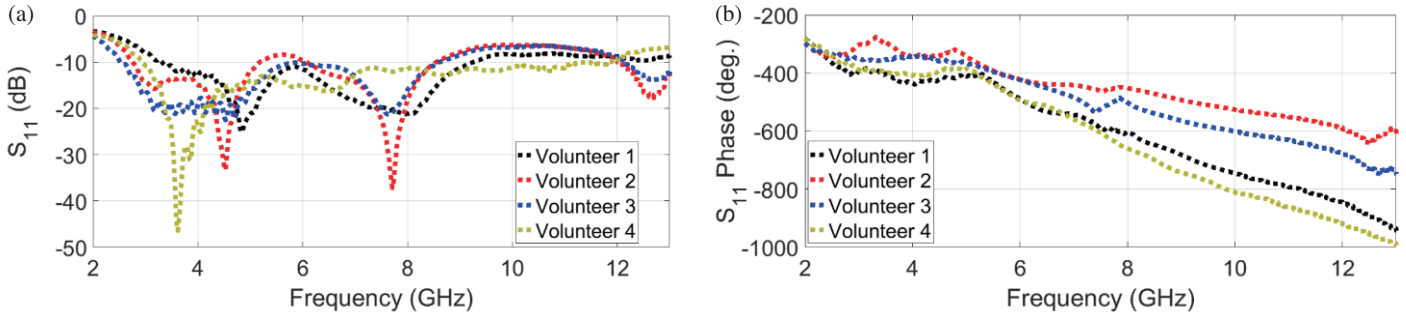

FIGURE 13. Measured reflection coefficients versus frequency for different levels of osteoporosis. (a) Magnitude. (b) Phase.

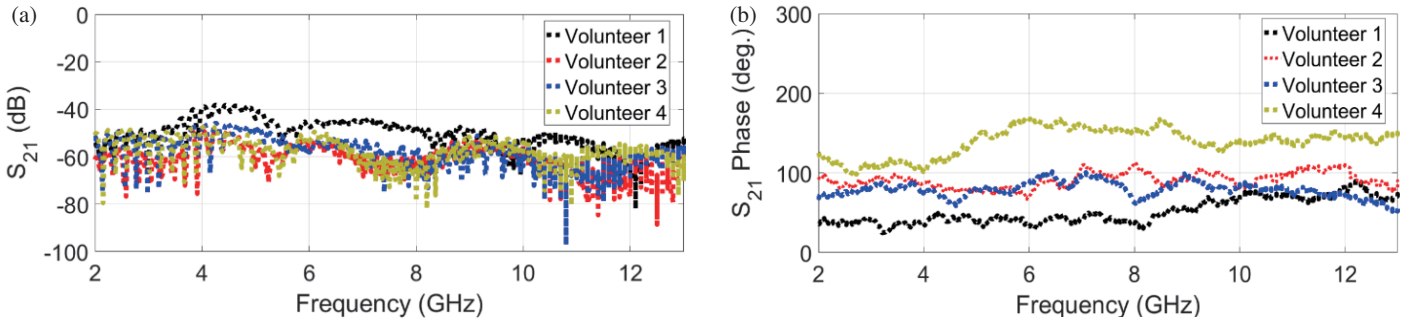

FIGURE 14. Measured trsnsmission coefficients versus frequency for different levels of osteoporosis. (a) Magnitude. (b) Phase.

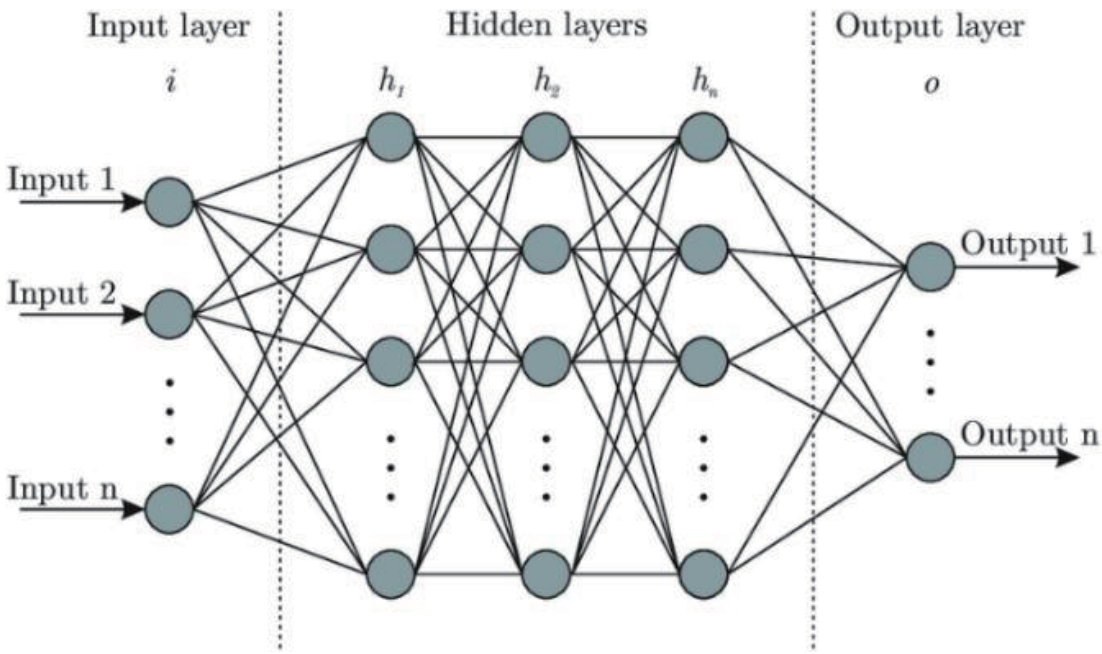

FIGURE 15. The structure of the artificial neural network.

enabling the neural network to predict the severity of osteoporosis based on the input data.

The forward propagation in the neural network can be expressed mathematically as follows:

$$\begin{aligned} Z^{[1]} &= W^{[1]}X+b^{[1]} \\ A^{[1]} &= ReLU(Z^{[1]}) \\ Z^{[2]} &= W^{[2]}X+b^{[2]} \\ A^{[2]} &= ReLU(Z^{[2]}) \\ Z^{[L]} &= W^{[L]}A^{[L-1]}+b^{[L]} \\ \hat{Y} &= softmax(Z^{[L]}) \end{aligned}$$

where X represents the input features; $W^{[l]}$ and $b^{[l]}$ are the weights and biases of layer l; $ReLU$ is the rectified linear activation function; and softmax computes the class probabilities.

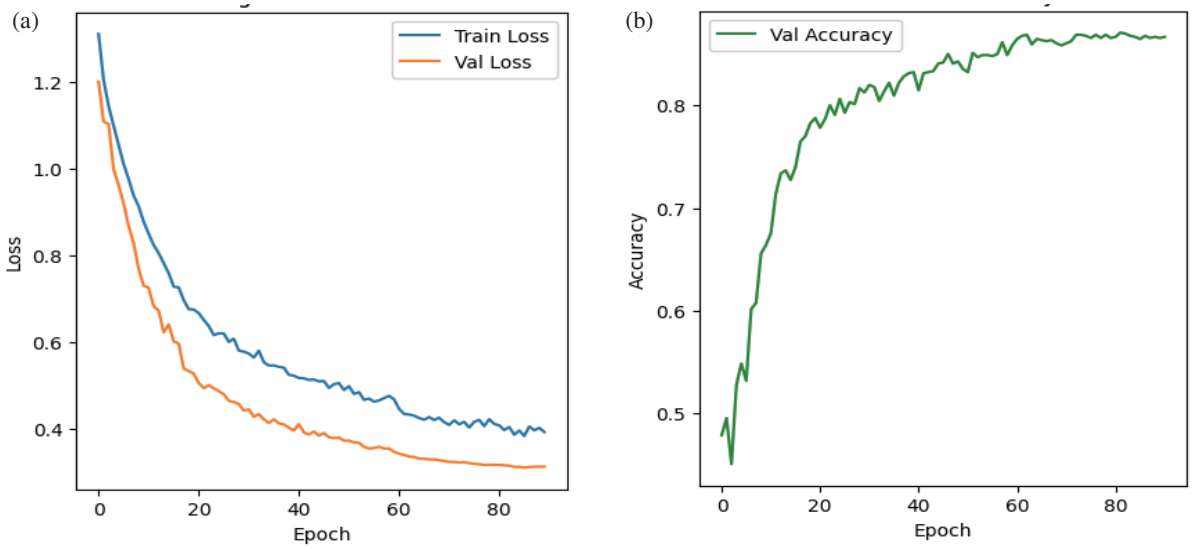

FIGURE 16. Neural network performance results. (a) The training and validation loss. (b) The validation accuracy.

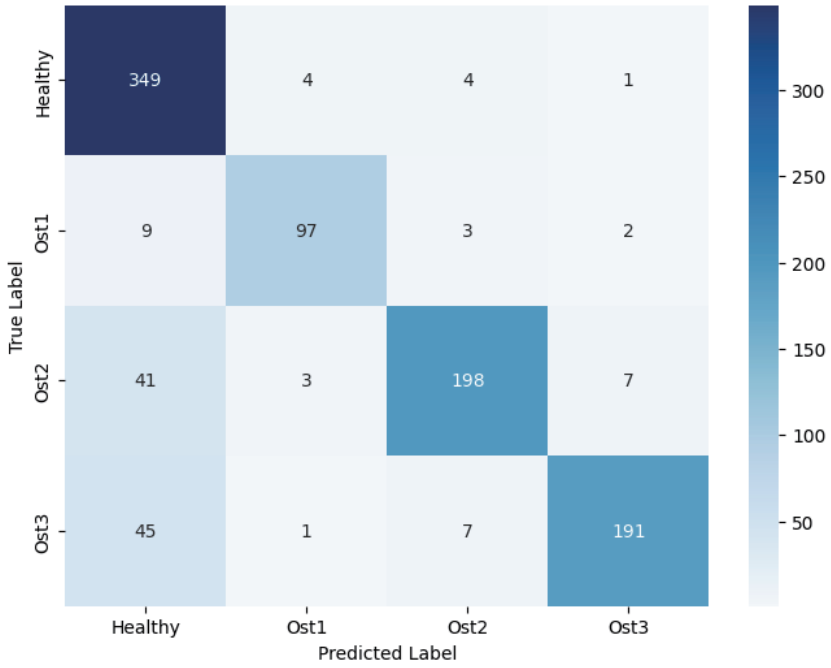

FIGURE 17. Confusion matrix.

5.3. Training the Model

The training process of the neural network involves iterative optimization of the model parameters to reduce the cross-entropy loss function. Seventy-five percent of the dataset is devoted to the training set, fifteen percent to the validation set, and fifteen percent to the testing set. This division ensures a balanced representation of samples across the datasets, facilitating robust model training and evaluation. Early stopping and learning rate scheduling strategies are used in training to enhance model convergence and avoid overfitting. Early stopping monitors for loss of validation and halts training if no progress is seen after a set number of epochs. Learning rate scheduling dynamically adjusts the learning rate based on the validation loss, facilitating efficient convergence towards an optimal solution.

Following training, in order to determine how well the trained model predicts osteoporosis levels, it is tested on the testing set. The accuracy metric is computed to quantify the percentage of correctly classified instances, providing insights into the model's effectiveness in real-world applications. It is possible to define the training process as an optimization problem, aiming to minimize the cross-entropy loss:

$$Loss = -\frac{1}{m}\sum_{i=1}^{m}\sum_{c=1}^{C}\left(y_i^{(c)}\log\left(\hat{y}_i^{(c)}\right)\right)$$

where m is the number of samples, c the number of classes, $y_i^{(c)}$ the true label, and $\hat{y}_i^{(c)}$ the predicted probability for class c.

5.4. Model Evaluation and Performance Visualization

Following training, we test the trained model's prediction of osteoporosis levels using the testing set. We compute the accuracy score, which measures the percentage of correctly classified instances. Additionally, we visualize the training and validation loss curves, as well as the validation accuracy curve as illustrated in Figure 16, to gain insights into the training progress and model performance.

The confusion matrix is presented in Figure 17 to assess a categorization model's performance. It depicts the four categories: Healthy, Ost.1, Ost.2, and Ost.3. Every cell within the matrix displays the count of model predictions against the actual labels. For instance, the top left cell shows that there are 349 instances where the model correctly predicted the 'Healthy' class. The darker shades along the diagonal from the left to the bottom right indicates higher numbers of correct predictions for each respective class, which is a positive indicator of model accuracy. Off-diagonal cells show misclassifications; for example, there are 41 instances where the model incorrectly predicted 'Ost.2' when the true class was 'Healthy'. The confusion matrix indicates a strong predictive performance for 'Healthy' and 'Ost.3' classifications, with acceptable confusion between 'Healthy' and 'Ost.2', suggesting possible areas for model improvement.

6. CONCLUSION

The integration of a novel wearable monopole antenna design, inspired by the intricate pattern of a Christmas snowflake, with advanced machine learning algorithms represents a transformative approach to osteoporosis detection and monitoring. This innovative system harnesses UWB electromagnetic waves and bone attenuation analysis to offer a noninvasive, compact, and highly accurate method for assessing bone health. The antenna design exhibits a good performance metrics, including an impedance bandwidth spanning 4.9 to 12.6 GHz and a reflection coefficient (S_{11}) consistently below -10 dB, all within a compact $41.9\,\text{mm} \times 29.2\,\text{mm}$ form factor. Through rigorous experimental validation and comparative studies, our research demonstrates the effectiveness of this integrated approach in accurately classifying osteoporosis levels. By leveraging machine learning algorithms to analyze reflections and transmission coefficients measured by the wearable system, we achieve high levels of accuracy in osteoporosis prediction, 87%. These findings represent a significant advancement in the field of wearable antennas and healthcare technology, offering new opportunities for early detection and personalized monitoring of osteoporosis. Furthermore, this research opens up promising avenues for innovative medical applications, contributing to the development of noninvasive tools for osteoporosis detection and diagnosis.

REFERENCES

[1] Choi, H. S., S. Y. Park, Y. M. Kim, S. H. Kim, K. M. Kim, and Y.-S. Chung, "Medical treatment of severe osteoporosis including new concept of advanced severe osteoporosis," *Osteoporosis and Sarcopenia*, Vol. 2, No. 1, 13–19, 2016.

[2] Aaseth, J., G. Boivin, and O. Andersen, "Osteoporosis and trace elements — An overview," *Journal of Trace Elements in Medicine and Biology*, Vol. 26, No. 2-3, 149–152, 2012.

[3] Delmas, P. D., "Treatment of postmenopausal osteoporosis," *The Lancet*, Vol. 359, No. 9322, 2018–2026, 2002.

[4] Cummings, S. R., W. Browner, D. M. Black, M. C. Nevitt, H. K. Genant, J. Cauley, K. Ensrud, J. .Scott, and T. M. Vogt, "Bone density at various sites for prediction of hip fractures," *The Lancet*, Vol. 341, No. 8837, 72–75, 1993.

[5] Babatunde, O. M., A. T. Fragomen, and S. R. Rozbruch, "Noninvasive quantitative assessment of bone healing after distraction osteogenesis," *HSS Journal*, Vol. 6, No. 1, 71–78, 2010.

[6] Kanis, J. A., L. J. M. III, C. Christiansen, C. C. Johnston, and N. Khaltaev, "The diagnosis of osteoporosis," *Journal of Bone and Mineral Research*, Vol. 9, No. 8, 1137–1141, 1994.

[7] Griffith, J. F., K. Engelke, and H. K. Genant, "Looking beyond bone mineral density: Imaging assessment of bone quality," *Annals of the New York Academy of Sciences*, Vol. 1192, No. 1, 45–56, 2010.

[8] Lang, T. F., G. Guglielmi, C. V. Kuijk, A. D. Serio, M. Cammisa, and H. K. Genant, "Measurement of bone mineral density at the spine and proximal femur by volumetric quantitative computed tomography and dual-energy x-ray absorptiometry in elderly women with and without vertebral fractures," *Bone*, Vol. 30, No. 1, 247–250, 2002.

[9] Gabriel, C., "The dielectric properties of biological tissues: III. Measurements in the frequency range 10 Hz to 20 GHz," *Phys. Med. Biol.*, Vol. 41, 2271–2293, 1996.

[10] Marzouk, H. M., A. S. A. E. Hameed, A. Allam, R. K. Pokharel, and A. B. A. Rahman, "A new rectangular dielectric resonator sensor for glucose measurement: Design, modeling, and experimental validation," *International Journal of Circuit Theory and Applications*, Vol. 52, No. 6, 3040–3051, 2024.

[11] Augustine, R., D. G. Kurup, S. Raman, D. Lee, K. Kim, and A. Rydberg, "Bone mineral density analysis using ultra wideband microwave measurements," in *2015 IEEE MTT-S International Microwave and RF Conference (IMaRC)*, 102–104, Hyderabad, India, 2015.

[12] Ghosh, D., A. De, M. C. Taylor, T. K. Sarkar, M. C. Wicks, and E. L. Mokole, "Transmission and reception by ultra-wideband (UWB) antennas," *IEEE Antennas and Propagation Magazine*, Vol. 48, No. 5, 67–99, 2006.

[13] Tlili, M., F. Deshours, G. Alquié, H. Kokabi, S. Hardinata, and F. Koskas, "Microwave resonant sensor for non-invasive characterization of biological tissues," *IRBM*, Vol. 39, No. 6, 445–450, 2018.

[14] Biswas, B., A. Karmakar, and V. Chandra, "Fractal inspired miniaturized wideband ingestible antenna for wireless capsule endoscopy," *AEU — International Journal of Electronics and Communications*, Vol. 120, 153192, 2020.

[15] Jagan, G., N. Palanikumar, A. Varun-Miranda, and S. Florence, "Development of a planar sensor for monitoring orthopaedic health," in *Proceedings of the 2016 IRF International Conference, Chennai, India*, 71–75, 2016.

[16] Cruz, A. S., S. G. Da Silva, and B. H. De Castro, "Bone density measurement through electromagnetic waves," in *The 6th 2013 Biomedical Engineering International Conference*, 1–5, Amphur

Muang, Thailand, 2013.

[17] Meaney, P. M., D. Goodwin, A. Golnabi, M. Pallone, S. Geimer, and K. D. Paulsen, "3D microwave bone imaging," in *2012 6th European Conference on Antennas and Propagation (EUCAP)*, 1770–1771, Prague, Czech Republic, 2012.

[18] Symeonidis, S., W. G. Whittow, C. Panagamuwa, and M. Zecca, "An implanted antenna system for the monitoring of the healing of bone fractures," in *2015 Loughborough Antennas & Propagation Conference (LAPC)*, 1–4, Loughborough, UK, 2015.

[19] Liang, J., C. C. Chiau, X. Chen, and C. G. Parini, "Study of a printed circular disc monopole antenna for UWB systems," *IEEE Transactions on Antennas and Propagation*, Vol. 53, No. 11, 3500–3504, Nov. 2005.

[20] Paracha, K. N., S. K. A. Rahim, P. J. Soh, and M. Khalily, "Wearable antennas: A review of materials, structures, and innovative features for autonomous communication and sensing," *IEEE Access*, Vol. 7, 56 694–56 712, Apr. 2019.

[21] Balanis, C. A., *Antenna Theory: Analysis and Design*, John Wiley & Sons, 2016.

[22] Wahab, M. G., A. S. A. El-Hameed, W. Swelam, and M. H. A. ElAzeem, "Design of miniaturized fractal quasi-self complimentary antenna for UWB applications," in *2016 IEEE International Symposium on Antennas and Propagation (APSURSI)*, 1809–1810, Fajardo, PR, USA, 2016.

[23] Abd El-Hameed, A. S., D. A. Salem, E. A. F. Abdallah, and E. A. Hashish, "Quasi self-complementary UWB notched microstrip antenna for USB application," *Progress In Electromagnetics Research B*, Vol. 56, 185–201, 2013.

[24] Abd El-Hameed, A. S., D. A. Salem, E. A. Abdallah, and E. A. Hashish, "Fractal quasi-self complimentary miniaturized UWB antenna," in *2013 IEEE Antennas and Propagation Society International Symposium (APSURSI)*, 15–16, Orlando, FL, USA, 2013.

[25] Alibakhshikenari, M., B. S. Virdee, P. Shukla, N. O. Parchin, L. Azpilicueta, C. H. See, R. A. Abd-Alhameed, F. Falcone, I. Huynen, T. A. Denidni, and E. Limiti, "Metamaterial-inspired antenna array for application in microwave breast imaging systems for tumor detection," *IEEE Access*, Vol. 8, 174 667–174 678, 2020.

[26] Lin, M. C., D. Hu, M. Marmor, S. T. Herfat, C. S. Bahney, and M. M. Maharbiz, "Smart bone plates can monitor fracture healing," *Scientific Reports*, Vol. 9, No. 1, 2122, 2019.

[27] Boologam, A. V., K. Krishnan, S. K. Palaniswamy, S. Kumar, S. Bhowmik, N. Sharma, D. Vaish, and S. Chatterjee, "On the design and development of planar monopole antenna for bone crack/void detection," *International Journal of Antennas and Propagation*, Vol. 2022, No. 1, 4663488, May 2022.

[28] Abd El-Hameed, A. S., D. M. Elsheakh, G. M. Elashry, and E. A. Abdallah, "A comparative study of narrow/ultra-wideband microwave sensors for the continuous monitoring of vital signs and lung water level," *Sensors*, Vol. 24, No. 5, 1658, 2024.

[29] Romeo, S., L. D. Donato, O. M. Bucci, I. Catapano, L. Crocco, M. R. Scarfì, and R. Massa, "Dielectric characterization study of liquid-based materials for mimicking breast tissues," *Microwave and Optical Technology Letters*, Vol. 53, No. 6, 1276–1280, 2011.

[30] Carey, J. J. and M. F. Delaney, "T-scores and Z-scores," *Clinical Reviews in Bone and Mineral Metabolism*, Vol. 8, 113–121, 2010.

[31] Balmer, T. W., S. Vesztergom, P. Broekmann, A. Stahel, and P. Büchler, "Characterization of the electrical conductivity of bone and its correlation to osseous structure," *Scientific Reports*, Vol. 8, No. 1, 8601, 2018.

[32] Amin, B., M. A. Elahi, A. Shahzad, E. Parle, L. McNamara, and M. O'Halloran, "An insight into bone dielectric properties variation: A foundation for electromagnetic medical devices," in *2018 EMF-Med 1st World Conference on Biomedical Applications of Electromagnetic Fields (EMF-Med)*, 1–2, Split, Croatia, 2018.

[33] Vendik, I. B., V. V. Pleskachev, V. Yakovlev, and S. Tamilova, "Microwave diagnostics of osteoporosis," in *2018 IEEE Conference of Russian Young Researchers in Electrical and Electronic Engineering (EIConRus)*, 1239–1242, Moscow and St. Petersburg, Russia, 2018.

[34] Andreuccetti, D., R. Fossi, and C. Perrucci, "Calculation of the dielectric properties of body tissues in the frequency range 10 Hz–100 GHz," IFAC-CNR, Florence (Italy) 1997-2015. http://niremf.ifac.cnr.it/tissprop/htmlclie/htmlclie.php.